Wavefield finite time focusing with reduced spatial exposure

Meles, Giovanni Angelo; Van Der Neut, Joost; Van Dongen, Koen W.A.; Wapenaar, Kees

DOI
10.1121/1.5110716

Publication date
2019

Document Version
Accepted author manuscript

Published in
Journal of the Acoustical Society of America

Citation (APA)
Meles, G. A., Van Der Neut, J., Van Dongen, K. W. A., & Wapenaar, K. (2019). Wavefield finite time focusing with reduced spatial exposure. *Journal of the Acoustical Society of America*, *145*(6), 3521-3530. https://doi.org/10.1121/1.5110716

Wavefield Finite Time Focusing with Reduced Spatial Exposure

Giovanni Angelo Meles[1 a)], Joost van der Neut[2], Koen W. A. van Dongen[2] and Kees Wapenaar[1]

[1]Faculty of Civil Engineering & Geosciences, Delft University of Technology, Delft, The Netherlands
[2]Faculty of Applied Sciences, Delft University of Technology, Delft, The Netherlands

[a)]e-mail: G.A.Meles@tu.delft.nl

Wavefield focusing is often achieved by Time-Reversal Mirrors, where wavefields emitted by a source located at the focal point are evaluated at a closed boundary and sent back, after Time-Reversal, into the medium from that boundary. Mathematically, Time-Reversal Mirrors are derived from closed-boundary integral representations of reciprocity theorems. In heterogeneous media, Time-Reversal Focusing theoretically involves in- and output signals that are infinite in time and the resulting waves propagate through the entire medium. Recently, integral representations have been derived for single-sided wavefield focusing. Although the required input signals for this approach are finite in time, the output signals are not and, similar to Time-Reversal Mirroring, the resulting waves propagate through the entire medium. Here, an alternative solution for double-sided wavefield focusing is derived. This solution is based on an integral representation where in- and output signals are finite in time, and where the energy of the waves propagating in the layer embedding the focal point is smaller than with Time-Reversal Focusing. We explore the potential of the proposed method with numerical experiments involving a head model consisting of a skull enclosing a brain.

I. INTRODUCTION

With Time-Reversal Mirrors, wavefields can be focused at a specified focal point in an arbitrary heterogeneous medium[1]. To realize such a mirror, wavefields from a source at the focal point are evaluated at a closed boundary and sent back, after Time-Reversal, into the medium from that boundary. As can be demonstrated from Green's theorem, this procedure leads to a solution of the homogeneous wave equation, consisting of an acausal wavefield that focuses at the focal point and a causal wavefield, propagating from the focal point through the entire medium to the boundary[2;3]. Applications can be found in various areas. In medical acoustics, Time-Reversal Mirroring has been applied for kidney stone and tumor ablation[4;5]. The Time-Reversal concept is also a key ingredient for various source localization[6;7] and reflection imaging[8;9] algorithms. Assuming that the medium is lossless and sufficiently heterogeneous, both the acausal wavefield that propagates towards the focal point and the causal wavefield that propagates through the medium to the boundary are unbounded in time.

Recently, it was shown that wavefields in one-dimensional media can also be focused from a single open-boundary by solving the Marchenko equation[10], being a familiar result from inverse scattering theory[11]. In this case a different focusing condition is achieved[12], and when the solution of the Marchenko equation is emitted into the medium from a single open-boundary, a focus emerges at the focal point, followed by a causal Green's function that propagates from the focal point through the entire medium to the boundary[13]. This result can be extended to three-dimensional wave propagation[14] and various focusing conditions[15] and has seen various applications in exploration geophysics, such as reflection imaging[16] and acoustic holography[17]. Although the focusing function is finite in time, the Green's function that emerges after wavefield focusing has infinite duration. In this paper, it will be discussed how to craft a focusing wavefield that, once injected in the medium from two open-boundaries, propagates to a specified focal point in finite time, without being followed by any Green's function. It will also be discussed how this focusing method theoretically reduces wavefield propagation in the layer which embeds the focal point. Numerical tests involving a complex model will show that wavefield propagation is largely reduced in the layer embedding the focal point despite the fact that exact focusing functions cannot be retrieved.

II. THEORY

Coordinates in three-dimensional space are defined as $\mathbf{x} = (x_1, x_2, x_3)$, and t denotes time. Although the derived theory can be modified for various types of wave phenomena, acoustic wave propagation is considered. The medium is lossless and characterized by propagation velocity $c\,(\mathbf{x})$ and mass density $\rho\,(\mathbf{x})$. It is assumed that these properties are independent of time. The acoustic pressure wavefield is expressed as $p\,(\mathbf{x}, t)$. For simplicity all derivations are carried out in the frequency domain, and the temporal Fourier transform of $p\,(\mathbf{x}, t)$ is defined by $p\,(\mathbf{x}, \omega) = \int_{-\infty}^{\infty} p\,(\mathbf{x}, t) \exp\,(i\omega t) dt$, where ω is the angular frequency. All wavefields obey the wave equation, which is defined in the frequency domain as

$$\partial_i \left(\frac{1}{\rho(\mathbf{x})} \partial_i p\,(\mathbf{x}, \omega) \right) + \frac{\omega^2}{\rho(\mathbf{x}) \mathrm{c}^2(\mathbf{x})} p\,(\mathbf{x}, \omega) = i\omega q\,(\mathbf{x}, \omega), \tag{1}$$

with ∂_i standing for the spatial derivative $\frac{\partial}{\partial x_i}$, where i takes the values $1, 2$ and 3. Einstein's summation convention is applied, meaning that summation is carried out over repeated indeces. Note that the source function $q\,(\mathbf{x}, \omega)$, standing for volume-injection rate density, is scaled by $i\omega$. Since the wave equation is often defined without this scaling factor elsewhere in the literature, the wavefields that appear in this paper should be divided with $(i\omega)$ to be consistent with that literature. The Green's function $G\,(\mathbf{x}, \mathbf{x}_S, \omega)$ is defined as the solution of the wave equation for $q\,(\mathbf{x}, \omega) = \delta\,(\mathbf{x} - \mathbf{x}_S)$, where $\mathbf{x}_S$ is the source location.

It has been shown how the real part of the Green's function with a source at $\mathbf{x}_A$ and a receiver at $\mathbf{x}_B$ can be expressed by integrating a specific combination of observations from sources at $\mathbf{x}_A$ and $\mathbf{x}_B$ over *any* boundary $\partial\mathbb{D}$ that encloses volume $\mathbb{D}$, where $\mathbf{x}_A \in \mathbb{D}$ and $\mathbf{x}_B \in \mathbb{D}$ (Fig. 1a):

$$\begin{aligned} &2\Re\{G\,(\mathbf{x}_B, \mathbf{x}_A; \omega)\} \\ &= \oint_{\partial\mathbb{D}} d^2\mathbf{x} \frac{1}{j\omega\rho(\mathbf{x})} \left(G\,(\mathbf{x}, \mathbf{x}_B, \omega)\, n_i \partial_i G^*\,(\mathbf{x}, \mathbf{x}_A, \omega) - G^*\,(\mathbf{x}, \mathbf{x}_A, \omega)\, n_i \partial_i G\,(\mathbf{x}, \mathbf{x}_B, \omega) \right), \end{aligned} \tag{2}$$

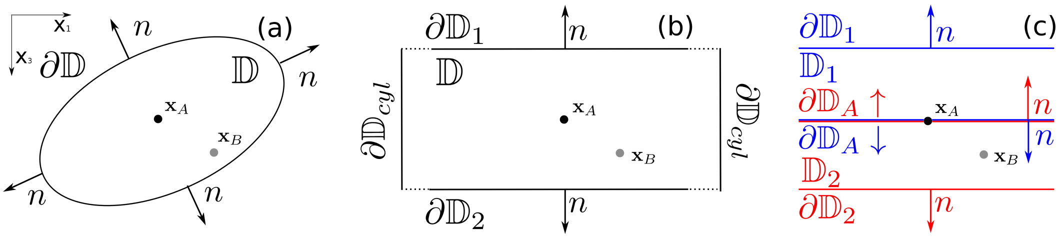

Figure 1: (Color online) (a) Cross-section of the configuration in the (x_1, x_3)-plane for Eq. (2). Volume $\mathbb{D}$ is enclosed by $\partial\mathbb{D}$ (solid line) with outward-pointing normal vectors n. (b) Cross-section of the configuration for Eq. (3). Volume $\mathbb{D}$ is enclosed by $\partial\mathbb{D}_1 \cup \partial\mathbb{D}_2 \cup \partial\mathbb{D}_{cyl}$ (solid black lines). (c) Cross-section of the configuration for Eq. (13) Volume $\mathbb{D}$ is splitted into $\mathbb{D}_1$ and $\mathbb{D}_2$, surrounded by $\partial\mathbb{D}_1 \cup \partial\mathbb{D}_A$ (blue line) and $\partial\mathbb{D}_2 \cup \partial\mathbb{D}_A$ (red line), respectively. Note that the normals n relative to $\partial\mathbb{D}_1 \cup \partial\mathbb{D}_A$ and $\partial\mathbb{D}_2 \cup \partial\mathbb{D}_A$ across $\partial\mathbb{D}_A$ are antiparallel. The focal point is at $\mathbf{x_A} \in \partial\mathbb{D}_\mathbf{A}$.

where n_i is the outward pointing normal of $\partial\mathbb{D}$ and superscript $*$ denotes complex conjugation. We call Eq. (2) a representation of the Green's function $G(\mathbf{x_B}, \mathbf{x_A}; \omega)$. In Time-Reversed acoustics, observations from a source at $\mathbf{x}_A$ are reversed in time and injected into the medium at $\partial\mathbb{D}$. The complex-conjugate Green's function $G^*(x, x_A, \omega)$ stands for the Fourier transform of the time-reversed observations. Equation (2) can thus be interpreted as if the injected field were propagated forward in time to any location $\mathbf{x}_B$ by the Green's function $G\left(\mathbf{x}_B, \mathbf{x}, \omega\right)$, which is equal to $G\left(\mathbf{x}, \mathbf{x}_B, \omega\right)$ through source-receiver reciprocity[18]. As can be learned from Eq. (2), this procedure yields for any location $\mathbf{x}_B$ the real part of the Green's function $G\left(\mathbf{x}_B, \mathbf{x}_A; \omega\right)$, which can be interpreted as the Fourier transform of the superposition of an acausal Green's function, focusing at $\mathbf{x} = \mathbf{x}_A$, and a causal Green's function that propagates from x_A through the entire medium to $\partial\mathbb{D}$. Since the source functions of this acausal and causal Green's function cancel each other, their superposition satisfies the homogeneous wave equation (i.e. Eq. (1) for $q\left(\mathbf{x}, \omega\right) = 0$). Note that this homogeneous wave equation is valid also for heterogeneous media. Note also that Time-Reversed acoustics results in a wavefield that at time $t = 0$ is non-zero just at the focal point[19], but it poses no constraints on the wavefield at other times.

We also consider a peculiar closed boundary $\partial\mathbb{D} = \partial\mathbb{D}_1 \cup \partial\mathbb{D}_2 \cup \partial\mathbb{D}_{cyl}$, where $\partial\mathbb{D}_1$ and $\partial\mathbb{D}_2$ are horizontal boundaries connected by a cylindrical surface $\partial\mathbb{D}_{cyl}$ with infinite radius (Fig. 1b). For this configuration, the contribution of the integral in Eq. (2) over $\partial\mathbb{D}_{cyl}$ vanishes and the following representation holds[17]:

$$2\Re\{G(\mathbf{x}_B,\mathbf{x}_A;\omega)\}$$
$$= \int_{\partial\mathbb{D}_1\cup\partial\mathbb{D}_2} d^2\mathbf{x}\frac{1}{j\omega\rho(\mathbf{x})}\left(G(\mathbf{x},\mathbf{x}_B,\omega)\, n_3\partial_3 G^*(\mathbf{x},\mathbf{x}_A,\omega) - G^*(\mathbf{x},\mathbf{x}_A,\omega)\, n_3\partial_3 G(\mathbf{x},\mathbf{x}_B,\omega)\right). \tag{3}$$

In addition to standard Time-Reversed acoustics, interesting focusing wavefields can be derived also by using focusing functions, which have recently been introduced to denote the solutions of the multidimensional Marchenko equation[14]. In this derivation, the same horizontal boundaries $\partial\mathbb{D}_1$ and $\partial\mathbb{D}_2$ as in Eq. (3) are used, but an additional auxiliary boundary $\partial\mathbb{D}_A$ is introduced. Here, $\partial\mathbb{D}_A$ is a horizontal plane inside $\mathbb{D}$ that intersects with the focal point $\mathbf{x}_A = (x_{1,A}, x_{2,A}, x_{3,A})$, so that volume $\mathbb{D}$ is divided into a subvolume $\mathbb{D}_1$, located above $\partial\mathbb{D}_A$, and a subvolume $\mathbb{D}_2$, located below $\partial\mathbb{D}_A$ (Fig. 1c). Note that the normals along $\partial\mathbb{D}_A$ associated with subvolumes $\mathbb{D}_1$ and $\mathbb{D}_2$ are antiparallel (Fig. 1c).

We deduce new sets of representation theorems for volumes $\mathbb{D}_1$ and $\mathbb{D}_2$. First of all, a reciprocity theorem of the convolution type[18] associated with volume $\mathbb{D}_1$ is introduced:

$$\int_{\mathbb{D}_1} d^3\mathbf{x}\,(p_A q_B - p_B q_A) = \int_{\partial\mathbb{D}_1} d^2\mathbf{x}\frac{1}{j\omega\rho}\left(p_B n_3\partial_3 p_A - p_A n_3\partial_3 p_B\right) - \int_{\partial\mathbb{D}_A} d^2\mathbf{x}\frac{2}{j\omega\rho}\left(p_A^+\partial_3 p_B^- + p_A^-\partial_3 p_B^+\right). \tag{4}$$

Subscripts A and B indicate two states. The integral over $\partial\mathbb{D}_A$ has been modified by using fundamental properties[20] of the (Helmholtz) operator in Eq. (2), where the wavefields have been decomposed into downgoing (indicated by superscript $+$) and upgoing (indicated by superscript $-$) constituents. In addition, the field has been normalized such that $p = p^+ + p^-$. Similarly, a reciprocity theorem of the correlation type[21] can be modified as

$$\int_{\mathbb{D}_1} d^3\mathbf{x}\,(p_A^* q_B + p_B q_A^*) = \int_{\partial\mathbb{D}_1} d^2\mathbf{x}\frac{1}{j\omega\rho}\left(p_B n_3\partial_3 p_A^* - p_A^* n_3\partial_3 p_B\right) - \int_{\partial\mathbb{D}_A} d^2\mathbf{x}\frac{2}{j\omega\rho}\left(p_A^{+*}\partial_3 p_B^+ + p_A^{-*}\partial_3 p_B^-\right). \tag{5}$$

Two representations will be derived for subvolume $\mathbb{D}_1$. In both representations, state A is source-free ($q_A = 0$). The medium properties in this state are identical to the physical properties $c(\mathbf{x})$ and $\rho(\mathbf{x})$ within $\mathbb{D}_1$, and can be arbitrarily set below $\partial\mathbb{D}_A$[14]. Here, the properties of the medium are chosen such that the halfspace below $\partial\mathbb{D}_A$ is non-scattering. A particular solution of the source-free wave equation will be substituted in this state, which is referred to as focusing function $p_A = f_1(\mathbf{x},\mathbf{x}_A,\omega)$, where $\mathbf{x}_A$ is the focal point and $\mathbf{x}$ is a variable coordinate inside the domain $\mathbb{D}$[14]. This focusing function is subject to a different focusing condition than what is achieved by Time-Reversed acoustics. In this paper, the condition is defined as $f_1^+(\mathbf{x}, \mathbf{x}_A; \omega)|_{\mathbf{x}\in\partial\mathbb{D}_A} = \delta(\mathbf{x}_H - \mathbf{x}_{H,A})$, where $\mathbf{x}_H = (x_1, x_2)$ is a point in the focal plane, while $f_1^-(\mathbf{x}, \mathbf{x}_A; \omega)|_{\mathbf{x}\in\partial\mathbb{D}_A}$ vanishes.

The first condition states that the downgoing part of the focusing function focuses at $\mathbf{x}_A$ not followed by any other event. This is achieved by cancelling any further down-going wave via destructive interference with propagation of the coda of the focusing function (see[14] for more details). After having focused, this downgoing function continues its propagation into the lower half-space. Since the lower half-space was chosen to be scattering-free, the upgoing part of the focusing function at $\partial\mathbb{D}_A$ is zero. Note that this condition does not pose any constraint on the wavefield at time $t = 0$ away from the focal plane $\partial\mathbb{D}_A$. In state B, the medium properties are equivalent to the physical medium, where an impulsive source is located at $\mathbf{x}_B \in \mathbb{D}$, yielding $q_B = \delta(\mathbf{x} - \mathbf{x}_B)$ and $p_B = G(\mathbf{x}, \mathbf{x}_B; \omega)$. Substituting these quantities into Eqs. (4) and (5) brings

$$\begin{aligned}\theta(x_{3,A} - x_{3,B}) f_1(\mathbf{x}_B, \mathbf{x}_A; \omega) + \frac{2}{j\omega\rho(\mathbf{x_A})}\partial_3 G^-(\mathbf{x}_A, \mathbf{x}_B, \omega) = \int_{\partial\mathbb{D}_1} d^2\mathbf{x} \frac{1}{j\omega\rho(\mathbf{x})} \times \\ \left(G(\mathbf{x}, \mathbf{x}_B, \omega) n_3 \partial_3 f_1(\mathbf{x}, \mathbf{x}_A, \omega) - f_1(\mathbf{x}, \mathbf{x}_A, \omega) n_3 \partial_3 G(\mathbf{x}, \mathbf{x}_B, \omega)\right),\end{aligned} \tag{6}$$

and

$$\begin{aligned}\theta(x_{3,A} - x_{3,B}) f_1^*(\mathbf{x}_B, \mathbf{x}_A; \omega) + \frac{2}{j\omega\rho(\mathbf{x_A})}\partial_3 G^+(\mathbf{x}_A, \mathbf{x}_B, \omega) = \int_{\partial\mathbb{D}_1} d^2\mathbf{x} \frac{1}{j\omega\rho(\mathbf{x})} \times \\ \left(G(\mathbf{x}, \mathbf{x}_B, \omega) n_3 \partial_3 f_1^*(\mathbf{x}, \mathbf{x}_A, \omega) - f_1^*(\mathbf{x}, \mathbf{x}_A, \omega) n_3 \partial_3 G(\mathbf{x}, \mathbf{x}_B, \omega)\right),\end{aligned} \tag{7}$$

where $\theta(x_3)$ is a Heaviside function, with $\theta(x_3) = 0$ for $x_3 < 0$, $\theta(x_3) = \frac{1}{2}$ for $x_3 = 0$ and $\theta(x_3) = 1$ for $x_3 > 0$.

Convolution and correlation reciprocity theorems associated with volume $\mathbb{D}_2$ are also introduced:

$$\int_{\mathbb{D}_2} d^3\mathbf{x}\,(p_A q_B - p_B q_A) = \int_{\partial\mathbb{D}_2} d^2\mathbf{x} \frac{1}{j\omega\rho}(p_B n_3 \partial_3 p_A - p_A n_3 \partial_3 p_B) + \int_{\partial\mathbb{D}_A} d^2\mathbf{x} \frac{2}{j\omega\rho}\left(p_A^+ \partial_3 p_B^- + p_A^- \partial_3 p_B^+\right), \tag{8}$$

$$\int_{\mathbb{D}_2} d^3\mathbf{x}\,(p_A^* q_B + p_B q_A^*) = \int_{\partial\mathbb{D}_2} d^2\mathbf{x} \frac{1}{j\omega\rho}(p_B n_3 \partial_3 p_A^* - p_A^* n_3 \partial_3 p_B) + \int_{\partial\mathbb{D}_A} d^2\mathbf{x} \frac{2}{j\omega\rho}\left(p_A^{+*} \partial_3 p_B^+ + p_A^{-*} \partial_3 p_B^-\right). \tag{9}$$

Two representations can be similarly derived for subvolume $\mathbb{D}_2$. For both representations, state A is source-free ($q_A = 0$), with medium properties as in the physical state in $\mathbb{D}_2$ and a non-scattering halfspace above $\partial\mathbb{D}_A$. Focusing function $p_A = f_2(\mathbf{x}, \mathbf{x}_A, \omega)$ will be substituted, being a solution of the source-free wave equation, with the focusing condition $f_2^-(\mathbf{x}, \mathbf{x}_A; \omega)\,|_{\mathbf{x}\in\partial\mathbb{D}_A} = \delta(\mathbf{x}_H - \mathbf{x}_{H,A})$, while $f_2^+(\mathbf{x}, \mathbf{x}_A; \omega)\,|_{\mathbf{x}\in\partial\mathbb{D}_A}$ vanishes. In state B, conditions are the same as in the derivation of the previous representations. Substituting these quantities into Eq. (8) and Eq. (9) yields

$$\begin{aligned}\theta(x_{3,B} - x_{3,A}) f_2(\mathbf{x}_B, \mathbf{x}_A; \omega) - \frac{2}{j\omega\rho(\mathbf{x_A})}\partial_3 G^+(\mathbf{x}_A, \mathbf{x}_B, \omega) = \int_{\partial\mathbb{D}_2} d^2\mathbf{x} \frac{1}{j\omega\rho(\mathbf{x})} \times \\ \left(G(\mathbf{x}, \mathbf{x}_B, \omega)\, n_3 \partial_3 f_2(\mathbf{x}, \mathbf{x}_A, \omega) - f_2(\mathbf{x}, \mathbf{x}_A, \omega)\, n_3 \partial_3 G(\mathbf{x}, \mathbf{x}_B, \omega)\right),\end{aligned} \tag{10}$$

and

$$\begin{aligned}\theta(x_{3,B} - x_{3,A}) f_2^*(\mathbf{x}_B, \mathbf{x}_A; \omega) - \frac{2}{j\omega\rho(\mathbf{x_A})}\partial_3 G^-(\mathbf{x}_A, \mathbf{x}_B, \omega) = \int_{\partial\mathbb{D}_2} d^2\mathbf{x} \frac{1}{j\omega\rho(\mathbf{x})} \times \\ \left(G(\mathbf{x}, \mathbf{x}_B, \omega)\, n_3 \partial_3 f_2^*(\mathbf{x}, \mathbf{x}_A, \omega) - f_2^*(\mathbf{x}, \mathbf{x}_A, \omega)\, n_3 \partial_3 G(\mathbf{x}, \mathbf{x}_B, \omega)\right).\end{aligned} \tag{11}$$

In the following we discuss two focusing strategies based on the focusing functions introduced in Eqs. (6)-(7) and (10)-(11).

Standard (double-sided) Marchenko Focusing can be achieved by injecting f_1 and f_2 from $\partial\mathbb{D}_1$ and $\partial\mathbb{D}_2$, respectively. The corresponding wavefields propagate from $\partial\mathbb{D}_1$ and $\partial\mathbb{D}_2$ to the focal point, subsequently generating scattering events in $\mathbb{D}_2$ and $\mathbb{D}_1$. Note that focusing functions f_1 and f_2 are defined in reference states involving non-scattering media below or above $\partial\mathbb{D}_A$[14], but in this physical experiment they are injected in the actual medium, thus generating scattering events below or above $\partial\mathbb{D}_A$. These scattered wavefields eventually interfere with the focal plane. Standard (double-sided) Marchenko Focusing can be mathematically expressed by the summation of Eqs. (6) and (10):

$$\begin{aligned}\theta(x_{3,A} - x_{3,B}) f_1(\mathbf{x}_A, \mathbf{x}_B; \omega) + \theta(x_{3,B} - x_{3,A}) f_2(\mathbf{x}_B, \mathbf{x}_A; \omega) + \\ \frac{2}{j\omega\rho(\mathbf{x_A})}\partial_3 G^+(\mathbf{x}_A, \mathbf{x}_B, \omega) - \frac{2}{j\omega\rho(\mathbf{x_A})}\partial_3 G^+(\mathbf{x}_A, \mathbf{x}_B, \omega) = \\ \int_{\partial\mathbb{D}_1} d^2\mathbf{x} \frac{1}{j\omega\rho(\mathbf{x})} \times \left(G(\mathbf{x}, \mathbf{x}_B, \omega)\, n_3 \partial_3 f_1(\mathbf{x}, \mathbf{x}_A, \omega) - f_1(\mathbf{x}, \mathbf{x}_A, \omega)\, n_3 \partial_3 G(\mathbf{x}, \mathbf{x}_B, \omega)\right) + \\ \int_{\partial\mathbb{D}_2} d^2\mathbf{x} \frac{1}{j\omega\rho(\mathbf{x})} \times \left(G(\mathbf{x}, \mathbf{x}_B, \omega)\, n_3 \partial_3 f_2(\mathbf{x}, \mathbf{x}_A, \omega) - f_2(\mathbf{x}, \mathbf{x}_A, \omega)\, n_3 \partial_3 G(\mathbf{x}, \mathbf{x}_B, \omega)\right),\end{aligned} \tag{12}$$

An additional focusing strategy can be derived by further inspection and manipulation of Eqs. (6)-(7) and (10)-(11). The different orientation of the normals along $\partial\mathbb{D}_A$ when associated with subvolumes $\mathbb{D}_1$ or $\mathbb{D}_2$ results in opposite signs of the Green's functions terms in the left-hand sides of Eqs. (6)-(7) and (10)-(11), respectively. Therefore, when Eq. (6), (7), (10) and (11) are added together, these Green's functions terms cancel out and it follows that:

$$2\Re\{f\left(\mathbf{x}_B,\mathbf{x}_A;\omega\right)\}$$
$$=\int_{\partial\mathbb{D}_1\cup\mathbb{D}_2} d^2\mathbf{x}\frac{1}{j\omega\rho\left(\mathbf{x}\right)}\left(G\left(\mathbf{x},\mathbf{x}_B,\omega\right)n_3\partial_3 2\Re\{f\left(\mathbf{x},\mathbf{x}_A,\omega\right)\}-2\Re\{f\left(\mathbf{x},\mathbf{x}_A,\omega\right)\}n_3\partial_3 G\left(\mathbf{x},\mathbf{x}_B,\omega\right)\right), \tag{13}$$

where

$$f\left(\mathbf{x},\mathbf{x}_A;\omega\right)=\theta\left(\mathbf{x}_{3,A}-\mathbf{x}_3\right)f_1\left(\mathbf{x},\mathbf{x}_A;\omega\right)+\theta\left(\mathbf{x}_3-\mathbf{x}_{3,A}\right)f_2\left(\mathbf{x},\mathbf{x}_A;\omega\right). \tag{14}$$

Akin to Eqs. (2) and (12), this result can be used for wavefield focusing. By injecting the real part of the wavefield $f\left(\mathbf{x},\mathbf{x}_A;\omega\right)$, as defined by Eq. (14), into the medium at boundaries $\partial\mathbb{D}_1$ and $\partial\mathbb{D}_2$, one can reconstruct this wavefield throughout the volume, as shown by Eq. (13). Due to the intrinsic properties of focusing functions, i.e. the destructive interference of the codas with up- and down-going reflections, any scattering event is confined within a spatial-temporal window defined by the propagation of the initial component of the focusing function (for more details see[14]). As a consequence, the wavefield in Eq. (13) propagates towards the focal point in finite time and back to the surface in finite time again.

Moreover, due to the focusing properties of f_1 and f_2, the wavefield f theoretically interacts with the focal plane $\partial\mathbb{D}_A$ only at $\mathbf{x}=\mathbf{x}_{H,A}$ at $t=0$. We refer to the focusing achieved by Eq. (13) as 'Finite Time Focusing with reduced spatial exposure', which we will often abbreviate as 'Finite Time Focusing'.

III. NUMERICAL EXAMPLES

For illustration purposes, the right-hand sides of Eqs. (2), (3), (12) and (13) are computed in a two-dimensional layered medium (Fig. 2(a)). The focusing function f_1 is retrieved using a standard configuation[23;22]. More precisely, iterative substitution of the coupled Marchenko equations allows to retrieve up- and down-going components of focusing functions associated with arbitrary locations in a medium. The methodology requires as input the single-sided reflection response at the acquisition surface and an estimate of the

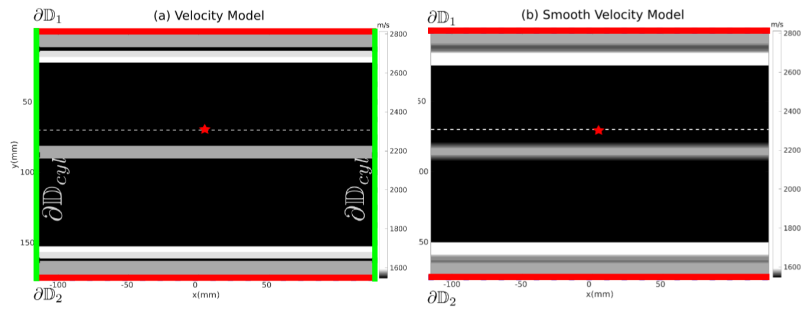

Figure 2: (Color online) (a) True velocity model used in the first numerical experiment, corresponding to a 1.5D model associated with a cross-line of a human head model (see Fig. 4 and Table 1). The red star and the dashed line represent the focal point and plane, respectively. For the Time-Reversal Focusing experiment associated with Eq. (2) (see the first column in Fig. 3), wavefields emanating from the focal point and recorded at evenly sampled receivers distributed along a closed boundary $\partial\mathbb{D}_1 \cup \partial\mathbb{D}_2 \cup \partial\mathbb{D}_{cyl}$ (thick red and green lines) are used. For the Time-Reversal Focusing experiment associated with Eq. (3) (see the second column in Fig. 3), only wavefields recorded along horizontal boundaries $\partial\mathbb{D}_1 \cup \partial\mathbb{D}_2$ (thick red lines) are used. For the focusing experiment associated with Eqs. (12) and (13) (see the third and fourth columns in Fig. 3), a total of evenly sampled 481×2 co-located sources and receivers (indicated by the thick red lines) are used to compute reflection data along the upper ($\partial\mathbb{D}_1$) and the lower ($\partial\mathbb{D}_2$) horizontal boundaries. Standard Marchenko methods are employed to retrieve focusing functions f_1 and f_2 using reflection data associated with $\partial\mathbb{D}_1$ and $\partial\mathbb{D}_2$, respectively[14]. (b) Smooth velocity model used to compute the initial focusing function emanating from the focusing point (red star) and recorded along the upper ($\partial\mathbb{D}_1$) and the lower ($\partial\mathbb{D}_2$) horizontal boundaries (thick red lines).

initial focusing function, i.e. the Time-Reversed direct wavefield from the specifed location in the subsurface to the acquisition surface. Here, to retrieve the focusing function f_1, reflection data are then collected along the *upper* boundary of the model ($\partial\mathbb{D}_1$ in Fig. 2(a)), while the estimate of the initial focusing function with a 0.8 MHz Ricker wavelet emanating from the focal point (red star in Fig. 2(b)) is computed in a smooth velocity model (see Fig. 2(b)). Similarly, the focusing function f_2 is retrieved using reflection data collected along the *lower* boundary of the model ($\partial\mathbb{D}_2$ in Fig. 2(a)). The estimate of the initial focusing function emanating from the focal point (red star in Fig. 2(b)) to the lower boundary receivers is also computed in the smooth velocity model in (Fig. 2(b)).

Note that all data used in this paper are computed using a Finite Difference Time Domain vector-acoustic forward solver[22].

The solutions (i.e., the left-hand sides) from Eqs. (2), (3), and (12) have infinite support in time, which could be disadvantageous for various applications. Things are different when Eq. (13) is considered: since the focusing functions f_1 and f_2 are confined in time and space by the direct propagation path from the boundary to the focal point[11], so is their superposition f. Hence, the solution associated with Eq. (13) seems preferable for wavefield focusing in finite time rather than those related to Eqs. (2), (3), and (12). More precisely, the real part of the focusing function f contains a series of wavefronts that are emitted into the medium from the upper and lower boundaries, and only the first of these wavefronts reaches the focal point. The remaining events are encoded such that any ingoing reflection of the first wavefront is canceled. The focusing conditions satisfied by Time-Reversed acoustics and Finite Time Focusing differ drastically with respect to wavefield propagation in the focal plane. While in Time-Reversed acoustics no constraint is posed on the propagation along the focal plane before or after time $t = 0$, Finite Time Focusing limits the interaction of the wavefield with the focal *plane* at the focal *point* and at time $t = 0$ only.

We illustrate this in Fig. 3 by showing propagation snapshots associated with the right-hand sides of Eqs. (2), (3), (12) and (13). Note that for the sake of brevity in the following we only focus on positive times, but identical considerations apply for the acausal components of the wavefields associated with Eqs. (2), (3), and (13), while no acausal Green's functions terms propagate in Eq. (12). In Time-Reversed acoustics, the superposition of an acausal and a causal Green's function focusing and propagating away from $\mathbf{x} = \mathbf{x}_A$, is expected (Eqs. (2) and (3)). Propagation around the foci is perfectly isotropic when Eq. (2) is used (green arrows in Figs. 3(a,e,i)), while the solution of Eq. (3) results in spurious events (black arrows in Fig. 3(b,f,j)) and artefacts, especially in the estimates of the direct wavefield along the focal plane (compare the amplitude of the wavefronts indicated by the green arrows in Figs. 3(e,i) and 3(f,j)). These low amplitude artefacts are due to the finite extent of the horizontal boundaries employed in our

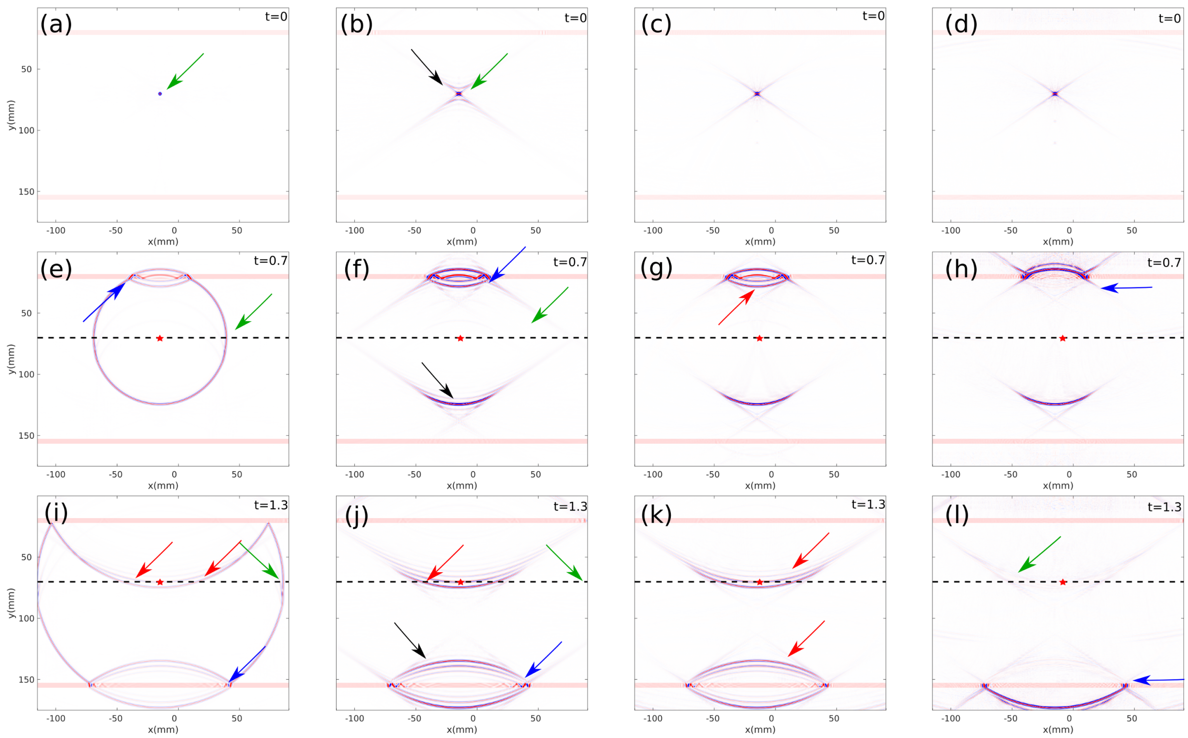

Figure 3: (Color online) First Column: Snapshots of the Time-Reversed solution when a closed boundary is considered (Eq. (2)). The focusing condition is satisfied, and the wavefield at time $t = 0$ is perfectly isotropic (green arrow). At time $t > 0$ direct (green arrows) as well as scattered (blue arrows) components of the wavefield are properly reconstructed. Red arrows indicate propagation of scattered waves through the focal plane. Light-red horizontal strips indicate strong reflectors, shown here for interpretation only, while the red star and the black dashed line stand for the focal point and plane, respectively. Second Column: Snapshots of the Time-Reversed solution when partial boundaries are considered (Eq. (3)). Due to the finite extent of the injection boundaries $\partial\mathbb{D}_1$ and $\partial\mathbb{D}_2$, the wavefield at time $t = 0$ is not perfectly isotropic (green arrow), and artefacts, with maximum amplitude $\sim 5\%$ of the focus magnitude, contaminate the wavefield throughout the entire simulation (black arrows). At times $t > 0$ scattered components of the wavefield are relatively well reconstructed (blue arrows), but the direct component of the wavefield exhibits distorted amplitudes along the horizontal direction (green arrows). Red arrows indicate propagation of scattered waves through the focal plane. Third Column: Snapshots corresponding to Standard (double-sided) Marchenko Focusing (Eq. (12)). The focusing condition is only satisfied at time $t = 0$ At times $t > 0$ scattered (red arrows) components of the wavefield are *not* suppressed by destructive interference with propagation of the coda of f. Fourth Column: Snapshots corresponding to Finite Time Focusing (Eq. 13). The focusing condition is satisfied except for low amplitude artefacts, with amplitude $\sim 2\%$ of the focus magnitude, propagating along the focal plane at times $t > 0$ (green arrows). Note that the wavefield at time $t = 0$ is not supposed to be vanishing throughout the domain (black arrows indicate propagation of the coda of f). At times $t > 0$ scattered (blue arrows) components of the wavefield are suppressed by destructive interference with propagation of the coda of f.

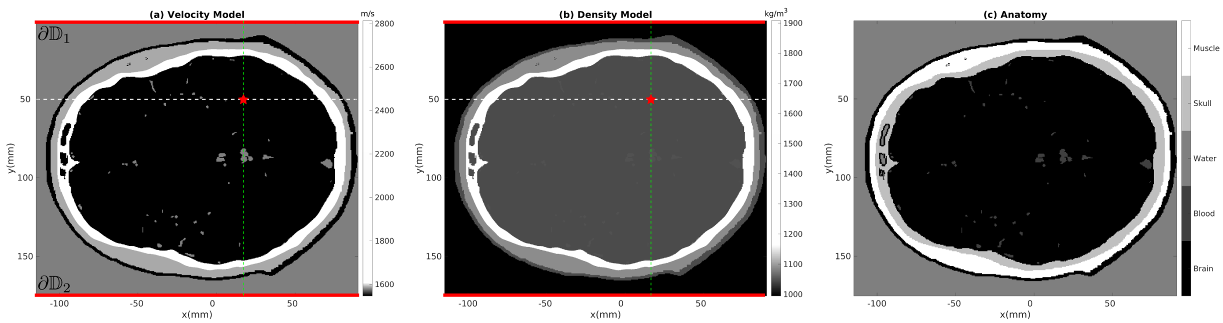

Figure 4: (Color online) (a) True velocity model used in the second numerical experiment. The red star and the gray dashed line represent the focal point and plane, respectively. The green line indicates the 1D profile used for the first numerical experiment. For the Time-Reversal Focusing experiment associated with Eq. (3) (see first columns of Figs. 5 and 6), wavefields emanating from the focal point and recorded at evenly spaced receivers located along horizontal boundaries $\partial\mathbb{D}_1 \cup \partial\mathbb{D}_2$ (thick red lines) are used. For the focusing experiments associated with Eqs. (12) and (13) (see second and third columns of Figs. 5 and 6), a total of 481×2 evenly sampled co-located sources and receivers (thick red lines) are used to compute reflection data along the upper ($\partial\mathbb{D}_1$) and the lower ($\partial\mathbb{D}_2$) horizontal boundaries. Standard Marchenko methods are employed to retrieve focusing functions f_1 and f_2 using reflection data associated with $\partial\mathbb{D}_1$ and $\partial\mathbb{D}_2$, respectively. This velocity model is also used to compute the initial focusing function emanating from the focal point (red star) and recorded along the upper ($\partial\mathbb{D}_1$) and the lower ($\partial\mathbb{D}_2$) horizontal boundaries (thick red lines). (b) True density model used in the second numerical experiments. (c) Anatomy of the brain used in the second numerical experiment. Keys as for (a).

numerical experiment when Eq. (3) is considered[19]. Note that in any case reflected waves propagating through the focal plane are well recovered both by Eqs. (2) and (3) (red arrows in Figs. 3(i) and 3(j)). In Standard (double-sided) Marchenko Focusing (Eq. (12)), focusing is achieved at time $t = 0$, but at later times Green's functions terms propagate within the layer embedding the focal plane (red arrows in Fig. 3(k)). In Finite Time Focusing, destructive interference of up- and down-going wavefields prevents primary as well as multiple reflections to propagate through the focal plane at any time (blue arrows in Fig. 3(h,l)). The interaction of the wavefield with the layer embedding the focal point is therefore limited to the propagation of the direct components of f. Note that no direct or scattered waves propagating from and to the acquisition surfaces interact with the focal *plane* except that at the focal *point*.

Tissue	velocity (m/s)	density (kg/m^3)
Muscle	1588	1090
Skull	2813	1908
Water	1578	994
Blood	1578	1050
Brain	1546	1046

Table 1: Velocity and density values for the head model used in the second experiment (see Fig. 4).

The theory and methodology presented here hold also for laterally variant models, and we show this by applying our focusing strategy to a second numerical experiment. In this case we consider a model consisting of a slice of a human head (see Fig. 4 and Table 1) and explore the applicability of the method to medical imaging/treatment[24]. This second example is chosen since it is particularly challenging for Marchenko focusing due to the presence of thin layers, diffractors and dipping layers[14]. As for the previous example, the focusing functions f_1 and f_2 are retrieved using standard Marchenko configurations, with reflection data collected along the upper and the lower boundaries of the model. Note that for actual therapy curved arrays are usually preferred over the linear acquisition configurations used here. The derivation of a new formulation of Finite Time Focusing to conform to more realistic therapeutical configurations will be the topic of future research. Initial focusing functions with a 0.8 MHz Ricker wavelet emanating from the focal point (red star in Fig. 4) to receivers at the upper and the lower boundaries are used. Note that for this example the initial focusing functions are computed in the true model (Fig. 4).

We first compare the focusing properties of solutions of Eqs. (3), (12) and (13) by showing in Figs. 5 and 6 snapshots of the corresponding wavefields associated with time intervals [0-0.4] s. and [1.2-1.6] s., respectively. Note that for the sake of brevity in the following we only focus on positive times, but identical considerations apply for the acausal components of the wavefields associated with Eqs. (3), and (13), while no acausal Green's functions terms propagate in Eq. (12). In Time-Reversed acoustics (first column in Fig. 5), the superposition of an acausal and a causal Green's function focusing and propagating away from $\mathbf{x} = \mathbf{x}_A$, is expected. However, due to the employed truncated boundaries, low amplitude artefacts occurring at time $t = 0$ contaminate the wavefield throughout the domain, especially in the proximity of the focal point (red arrows in Fig. 5(a)). Similar artefacts at time $t = 0$ also contaminate the wavefield associated with Eqs. (12) (second

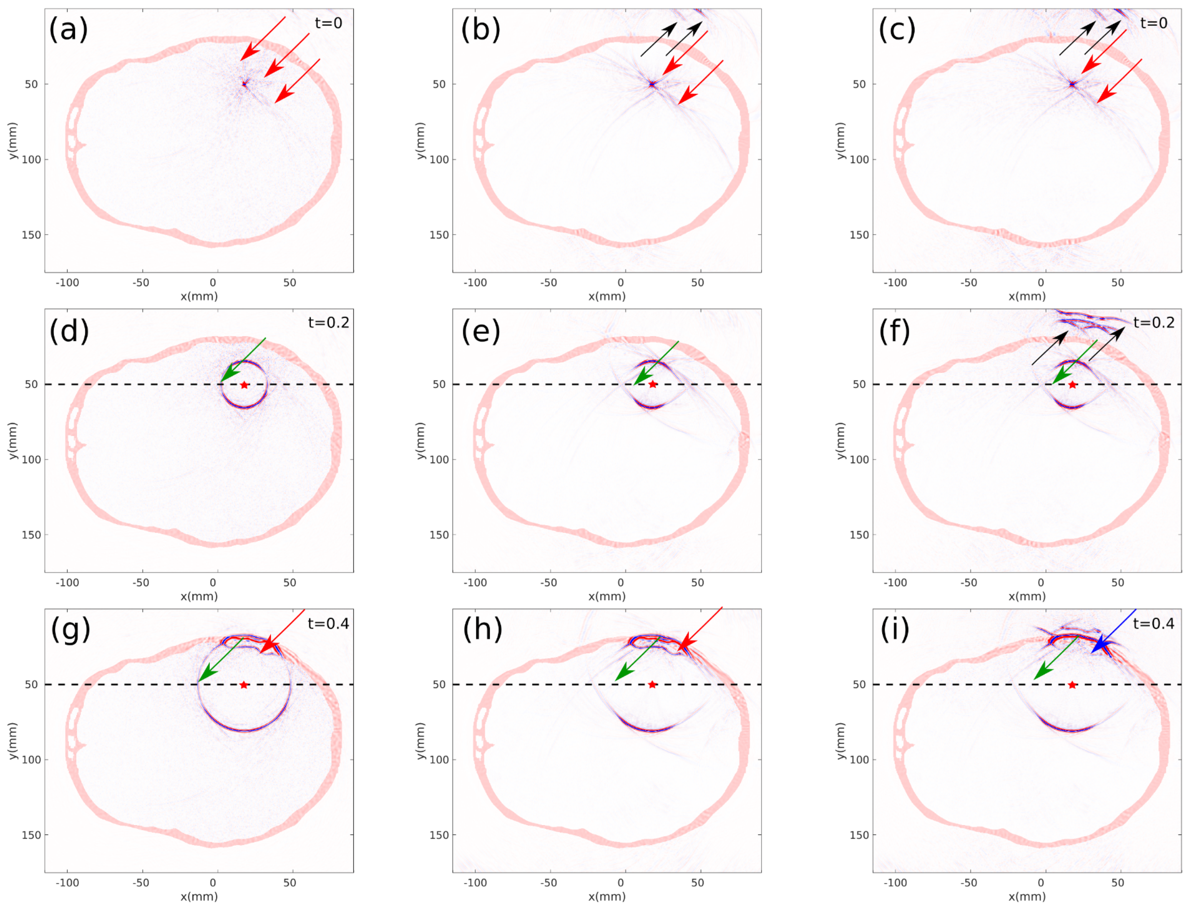

Figure 5: (Color online) Focusing properties of solutions of Eqs. (3), (12) and (13) in the time interval [0-0.4] s. First column: Snapshots of the Time-Reversed solution when partial boundaries are considered (Eq. (3)). Due to the finite extent of the injection boundaries $\partial\mathbb{D}_1$ and $\mathbb{D}_2$, small amplitude artefacts contaminate the wavefield at time $t = 0$ (red arrows in (a)). Due to the strong lateral reflections, at times $t > 0$ direct components of the wavefield are relatively well reconstructed (green arrows in (d) and (g)). The red arrow in (g) indicates a scattered wave reflected at the interface above the focal plane. Second column: Snapshots corresponding to Standard (double-sided) Marchenko Focusing (Eq. (12)). The focusing condition is satisfied except that for low amplitude artefacts, contaminating the domain at time $t = 0$ (red arrow in (b)). Note that the wavefield at time $t = 0$ is not supposed to be vanishing throughout the domain (black arrows indicate propagation of the coda of f). At times $t > 0$ scattered components of the wavefield are *not* attenuated by destructive interference with propagation of the coda of f (red arrow in (h)). Third column: Snapshots of the focusing in finite time with minimal spatial exposure solution (Eq. (13)). The focusing condition is satisfied except for low amplitude artefacts, contaminating the domain at time $t = 0$ (red arrow in (c)). Note that the wavefield at time $t = 0$ is not supposed to be vanishing throughout the domain (black arrows indicate propagation of the coda of f). At times $t > 0$ scattered components of the wavefield are attenuated by destructive interference with propagation of the coda of f (blue arrow in (i)). Keys as in Fig. 3.

.

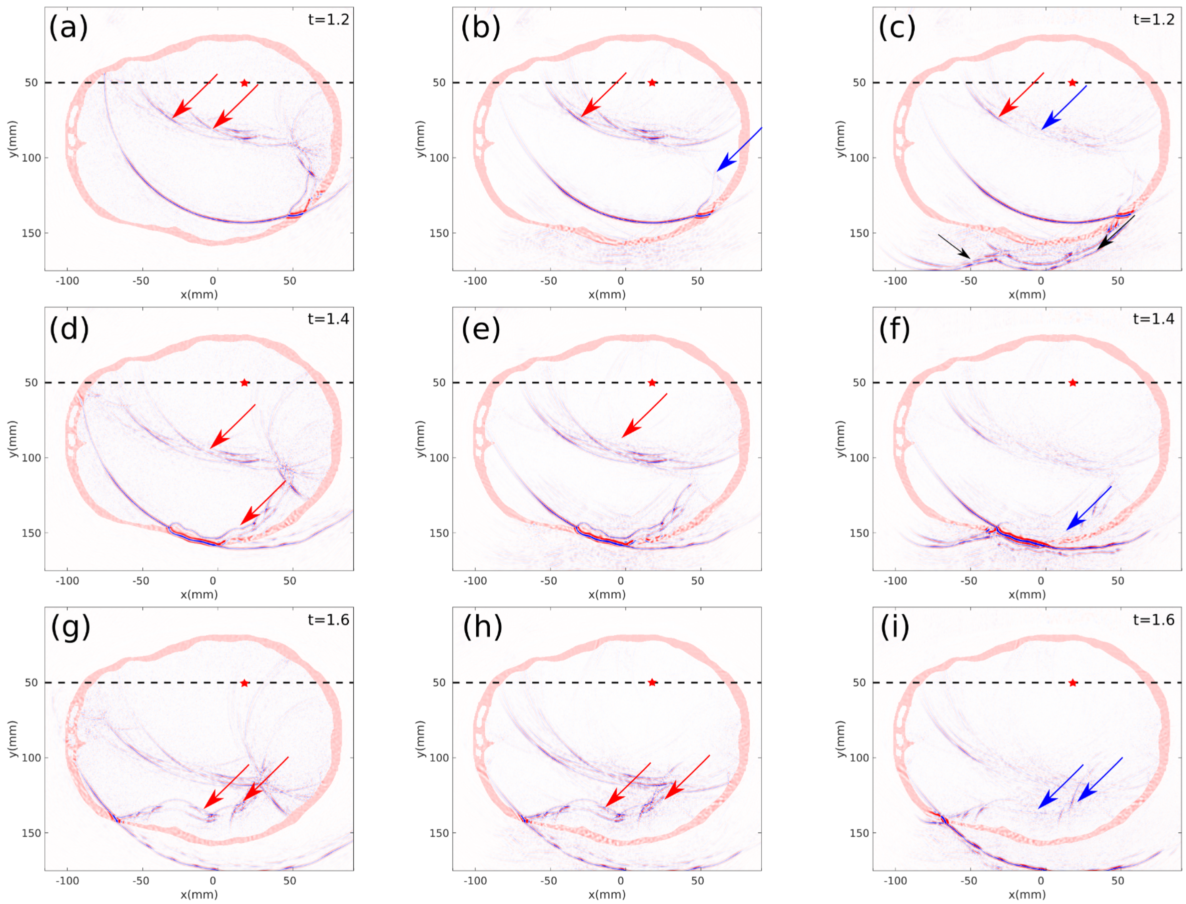

Figure 6: (Color online) Focusing properties of solutions of Eqs. (3), (12) and (13) in the time interval [1.2-1.6] s. First column: Snapshots of the Time-Reversed solution when partial boundaries are considered (Eq. (3)). Red arrows point at reflections with the skull walls. Second column: Snapshots corresponding to Standard (double-sided) Marchenko Focusing (Eq. (12)). The red arrows in (b, e, h) indicate scattered waves reflected at the interface above and below the focal plane. Third column: Snapshots of the focusing in finite time with minimal spatial exposure solution (Eq. (13)). Black and blue arrows point at the coda of the focusing functions and attenuated reflections, respectively. Keys as in Fig. 3.

column in Fig 5) and 13 (third column in Fig 5). In Figs. 5(d) and 5(g) the wavefield associated with Eq. (3) is shown to propagate almost isotropically around the focal point. More precisely, direct components of the wavefield $G(x_B, x_A)$, associated via Eq. (3) with laterally scattered waves $G(x, x_A)$ and $G(x, x_B)$[25], interact with the focal plane (green arrow in Fig. 5(d)) at positive times. By contrast, the wavefields associated with Eqs. (12) and (13) do not exhibit similar components (green arrows in Figs. 5(e,f,h,i)). The red arrow in Fig. 5(g) indicates a primary reflection associated with the wall of the skull above the focal plane. A similar event, corresponding to a Green's function term, is present Fig. 5(h). On the other hand, the coda of the focusing function (black arrows in Figs. 5(f)) interferes destructively with this reflection (blue arrow in Fig. 5(i)). Due to the complexity of the model, i.e., the presence of thin layers, diffractors and dipping layers[14], the cancellation of the ingoing reflection is not perfect (red arrows in Fig. 6(c)), but the amplitude of the reflected wave is generally *reduced* (blue arrow in Fig. 6(c)). Similar considerations apply also for the reflection associated with the wall of the skull below the focal plane, where again the coda of the focusing function (black arrows in Fig. 6(c)) is shown to interfere destructively (blue arrows in Figs. 6(f) and 6(i)) with the ingoing-reflection (red arrows in Figs. 6(g) and 6(h)).

The differences between the three discussed focusing strategies are visualized in another way in Fig. 7, where the L_2 norm of the pressure wavefields associated with Eqs. (3), (12) and (13) is plotted as a function of space. Note that all maps are normalized to allow proper comparison of the three focusing methods. In Standard Time-Reversal Focusing, the norm of the pressure wavefield exhibits a peak at the focal point (blue arrow in Fig. 7a), and significant values are almost homogeneously distributed throughout the brain (red arrows in Fig. 7(a)). This indicates that wave propagation occurs in the entire brain, which could be undesirable for medical treatments designed to target the focal point while not affecting other portions of the brain. Significant wavefield propagation throughout the brain occurs also when Standard (double-sided) Marchenko Focusing is employed (red arrows in Fig. 7(b)). The situation is rather different when focusing is achieved via solution of Eq. (13). Due to the peculiar focusing condition associated with Marchenko schemes[12], the corresponding wavefield still exhibits a peak at the focal point (blue arrow in Fig. 7(c)) while being mostly confined into a double cone centered at the focal point (blue cones in Fig. 7(c)). Black and green arrows point at regions of the brain with minimal wavefield propagation inside the brain and large amplitude spots outside the brain associated with the propagation of the coda of the focusing functions, respectively. The different performances of Time-Reversal, Standard (double-sided) Marchenko and Finite Time Focusing can be better appreciated in Figs. 7(d-e), where horizontal (d) and vertical (e) sections of the maps in Fig. 7(a-c) are plotted in Decibel scale ($20log_{10}(\|p\|)$). As expected, along the horizontal section (d) Finite Time Focusing exhibits reduced

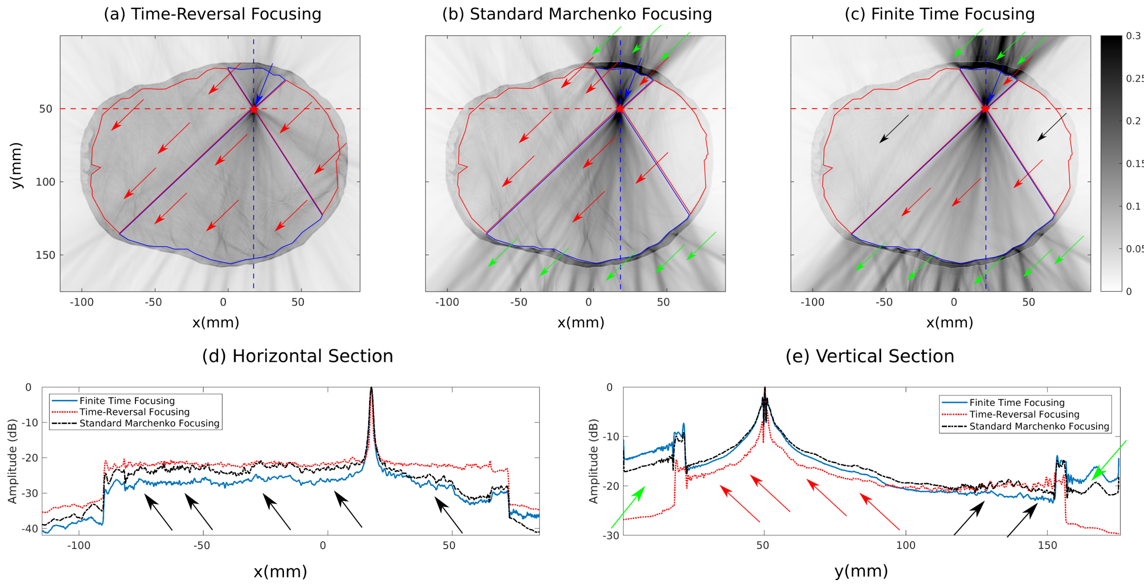

Figure 7: (Color online) Normalized L_2 norm of the pressure wavefields associated with the left-hand sides of Eqs. (3) (a), (12) (b) and (13) (c), respectively, plotted as functions of space. In Standard Time-Reversal Focusing (a), the norm of the pressure wavefield exhibits a peak at the focal point (blue arrow in a), and significant values are almost homogeneously distributed throughout the model (red arrows in (a)). A similar distribution, with large values along the focal plane, is obtained when Standard (double-sided) Marchenko Focusing is used (b). In Finite Time Focusing, the wavefield is still exhibiting a peak at the focal point (blue arrow in Fig. (c)) while being somehow confined into a double cone centered at the focal point (blue cones in (c)). Black and green arrows point at regions of the brain with minimal wavefield propagation and large amplitude spots associated with the propagation of the coda of the focusing functions, respectively. Red and blue dashed lines indicate horizontal and vertical sections used in (d-e), respectively. Horizontal (d) and vertical (e) slices of the maps in Fig. (a-c), plotted in Decibel scale ($20log_{10}(\|p\|)$). Black arrows in (d) indicate large portions of the focal plane (red dashed lines in (a-c)) where wavefield propagation in Finite Time Focusing is significantly reduced as opposed to Time-Reversal and Standard (double-sided) Marchenko Focusing. The red and black arrows in (e) indicate zones along the green dashed lines in Fig. (a-c) where Finite Time Focusing and Time-Reversal Focusing involves slightly larger and slightly smaller wavefield intensity, respectively. Green arrows point at zones outside of the skull where Standard (double-sided) Marchenko and Finite Time Focusing involve propagation of coda exhibiting large amplitudes (see green arrows in Fig. (c)). Keys as in Fig. 4.

	Brain	Blue Cones	Red Cones
SMF	+1%	+16%	-26%
FTF	-14%	+5%	-45%

Table 2: Norm differences of the wavefields associated with the two new focusing strategies discussed in this paper (Standard (double-sided) Marchenko Focusing, here SMF, and Finite Time Focusing, here FTF) in the whole brain, first column, in the blue cones, second column, and in the red cones, third column. Values are compared to the norm associated with Time-Reversal Mirroring in each domain.

wavefield propagation, whereas along the vertical direction (e) the three diagrams are rather similar. Note that in Time-Reversal Mirroring wavefield propagation across the focal plane occurs before and after time $t = 0$, in Standard (double-sided) Marchenko Focusing at time $t \geq 0$ and in Finite Time Focusing the interaction of the wavefield with the focal point theoretically takes place only at time $t = 0$. Therefore, in Time-Reversal Mirroring and Standard (double-sided) Marchenko Focusing the norm of the wavefield at the focal point is intrinsically associated with both direct and scattered waves, while in Finite Time Focusing it is theoretically only associated with direct components of the focusing function f. The overall focusing performances of the discussed methods are summarized in Table 2. The brain is divided in four domains, enclosed by the blue and the red curves in Figures 7(a-c), which represent cones converging to the focal plane from the horizontal (i.e. the acquisition surface) and the vertical sides of the model, respectively. The norm of the wavefields associated with the three focusing strategies discussed in this paper is computed in the whole brain and in the areas enclosed by the blue and red curves. Values are normalized with respect to the norms associated with Time-Reversal Mirroring in each individual domain. While in the whole brain and in the blue areas the three focusing strategies exhibit similar norm values, in the red areas Finite Time Focusing involves significantly smaller values than Time-Reversal Mirroring and Standard (double-sided) Marchenko Focusing.

IV. DISCUSSION

The wavefields resulting from the Time-Reversal and Standard (double-sided) Marchenko methods, as formulated by Eqs. (2), (3) and (12) have infinite support in time, which could be disadvantageous for various applications. Things are different in Finite Time Focusing (Eq. (13)), which involves wavefields that are confined in time and space by the direct propagation path from the boundary to the focal point. As can be observed in Figs. 3, 5, and 6, the real part of the focusing function f contains a series of wavefronts that once emitted into the medium from the surrounding boundary interfere destructively with any ingoing reflection of the first pulse. Even when perfect focusing is not achieved, the amplitude of ingoing reflections is at least suppressed. Hence, the focusing function might be an attractive solution of the wave equation for focusing below strong acoustic contrasts. By canceling or reducing the amplitude of ingoing reflections, we achieve the desirable situation of a single wavefront or reduced energy to reach the focal point and propagate along the focal plane. Moreover, the peculiar nature of the focusing achieved by Eq. (13) minimizes the spatial exposure to the incident wavefield of the layer embedding the focal point, and this could possibly be beneficial for sensitivity analysis and/or safety concern in medical treatment[26]. Focusing functions associated with Eq. (13) may also therefore be useful input for inversion. Akin to Green's functions, they obey the wave equation, which can be inverted for the medium properties $c(\mathbf{x})$ and $\rho(\mathbf{x})$. In particular cases, they may be preferred over Green's functions for this purpose, since the entire signals can be captured by a concise recording in the time domain and exhibit peculiar sensitivity distributions. In the numerical tests considered here, we used either kinematically equivalent (first numerical experiment) or exact velocity models (second numerical experiment) to compute the initial focusing functions. When a poor background model is used, solutions from above and below could focus at different points, and the terms associated with the Green's functions in Eqs. (6)-(7) and (10)-(11) would not cancel out, thus violating the focusing condition exhibited by f. Note that this restriction holds also for the Time-Reversal method when applied from two sides. The human skull involves some of the most critical challenges for Marchenko applications, i.e. the presence of thin layers, diffractors, dipping layers and strong absorption. In our numerical test an acoustic and loseless model was employed. Note that using a lossless head model allowed us to test the method on a simplified and yet very challenging problem. However, neglecting dissipation, which plays a key role in medical treatment, limits the immediate applicability of the current algorithm of Finite Time Focusing, and a new theoretical framework to include absorption needs to be devised. Recent research has shown that when media are accessible from two sides (which is a strict requirement in the focusing strategy discussed in this paper), Marchenko redatuming can be adapted to account for dissipation[27], and these insights could foster future research devoted to extension of the proposed method to account for dissipative media.

V. CONCLUSIONS

A new integral representation has been derived for wavefield focusing in an acoustic medium. Unlike in the classical representation for this problem based on Time-Reversed acoustics, the input and output signals for this type of focusing are finite in time and only involve propagation of direct waves in the layer that embeds the focal point. This leads to a reduction of spatial and temporal exposure when wavefield focusing is applied in practice. The method has been validated numerically for a head model consisting of hard (skull) and soft (brain) tissue. There results confirm that the proposed method can outperform classical Time-Reversed acoustics.

VI. ACKNOWLEDGMENTS

This work is partly funded by the European Research Council (ERC) under the European Union's Horizon 2020 research and innovation programme (grant agreement No: 742703). The authors thank Associate Editor Dr. Yun Jing and two anonymous reviewers, whose comments have helped us improving our manuscript. Joost van der Neut is also grateful to Niels Grobbe (University of Hawaii) for stimulating discussions and for conducting some of the initial research that evolved into this contribution.

REFERENCES

1. M. Fink, Journal of Physics D: Applied Physics, *Time-reversal mirrors*, **26**, 1333-1350 (1993).

2. K. Wapenaar, E. Slob and R. Snieder, Physical Review Letters, *Unified Green's function retrieval by cross correlation* **97**, 234301 (2006).

3. M. Fink, Geophysics, *Time-reversal acoustics in complex environments*, **71**, SI151-SI164 (2006).

4. J. L. Thomas, F. Wu and M. Fink, Ultrasonic imaging, *Ultrasonic beam focusing through tissue inhomogeneities with a time reversal mirror: application to transskull therapy*, **18**, 106-121 (1996).

5. J. F. Aubry, M. Pernot, M. Tanter, G. Montaldo and M. Fink, *Ultrasonic arrays: New therapeutic developments*, Journal de Radiologie, **88**, 1801-1809 (2007).

6. S. Catheline, M. Fink, N. Quieffin and R. J. Ing, Applied Physics Letters, *Acoustic source localization model using in-skull reverberation and time reversal*, **90**, 063902 (2007).

7. Li, Z. and M. van der Baan, Geophysics, *Microseismic event localization by acoustic time reversal extrapolation*, **81**, JS123-KS134 (2016).

8. G.A. McMechan, Geophysical Prospecting, *Migration by extrapolation of time-dependent boundary values*, **31**, 413-420 (1983).

9. M. K. Oristaglio, Inverse Problems, *An inverse scattering formula that uses all the data*, **5**, 1097-1105 (1989).

10. J. H. Rose, Inverse Problems, *Single-sided autofocusing of sound in layered media*, **18**, 1923-1934 (2002).

11. R. Burridge, Wave Motion, *The Gelfand-Levitan, the Marchenko and the Gopinath-Sondhi integral equations of inverse scattering theory, regarded in the context of inverse impulse-response problems*, **2**, 305-323 (1980).

12. K. Wapenaar, and J. Thorbecke, Geophysical Prospecting, *Virtual sources and their responses, Part I: time-reversal acoustics and seismic interferometry*, **65**, 1411-1429 (2017).

13. F. Broggini and R. Snieder, European Journal of Physics, *Connection of scattering principles: A visual and mathematical tour*, **33**, 593-613 (2012).

14. K. Wapenaar, J. Thorbecke, J. van der Neut, F. Broggini, E. Slob, and R. Snieder, Journal of the Acoustical Society of America, *Green's function retrieval from reflection data, in absence of a receiver at the virtual source position*, **135**, 2847-2861 (2014).

15. G.A. Meles, K. Wapenaar, J. Thorbecke, Geophysical Journal International, *Virtual plane-wave imaging via Marchenko redatuming*, **214**, 508-519 (2018).

16. M. Ravasi, I. Vasconcelos, A. Kritski, A. Curtis, C. Alberto da Costa Filho, and G. Meles, Geophysical Journal International, *Target-oriented Marchenko imaging of a North Sea field*, **205**, 99-104 (2016).

17. K. Wapenaar, J. Thorbecke and J. van der Neut, Geophysical Journal International, *A single-sided homogeneous Green's function representation for holographic imaging, inverse scattering, time-reversal acoustics and interferometric Green's function retrieval*, **205**, 531-535 (2016).

18. J. T. Fokkema and P. M. van den Berg, Elsevier Science Publishing Company, *Seismic Applications of Acoustic Reciprocity*, Inc. (1993).

19. K. Wapenaar, J. Thorbecke, J. van der Neut, E. Slob and R. Snieder, Geophysical Prospecting, *Virtual sources and their responses, Part II: data-driven single-sided focusing*, **65**, 1430-1451 (2017).

20. L. Fishman, Radio Science, *Oneway wave propagation methods in direct and inverse scalar wave propagation modeling*, **28**, 865-876 (1993)

21. N. N. Bojarski, Journal of the Acoustical Society of America, *Generalized reaction principles and reciprocity theorems for the wave equations, and the relationship between the timeadvanced and timeretarded fields*, **74**, 281-285 (1983).

22. J. Thorbecke, E. Slob, J. Brackenhoff, J. van der Neut and K. Wapenaar, Geophysics, *Implementation of the Marchenko method*, **82**, WB29-WB45 (2017).

23. J. van der Neut, I. Vasconcelos and K. Wapenaar, Geophysical Journal International, *On Green's function retrieval by iterative substitution of the coupled Marchenko equations*, **203**, 792813 (2015).

24. M. I. Iacono, E. Neufeld, E. Akinnagbe, K. Bower, J. Wolf, I.V. Oikonomidis, D. Sharma, B. Lloyd, B.J. Wilm, M. Wyss, and K. P. Pruessmann, PloS one, *MIDA: A Multimodal Imaging-Based Detailed Anatomical Model of the Human Head and Neck*, **10**, 0124126 (2015).

25. R. Snieder, K. Wapenaar, K. Larner, Geophysics, *Spurious multiples in seismic interferometry of primaries*, **71**, SI111-SI124 (2006).

26. A. Hughes, K. Hynynen, Physics in Medicine & Biology, *Design of patient-specific focused ultrasound arrays for non-invasive brain therapy with increased trans-skull transmission and steering range*, **17**, L9-L19 (2017).

27. E. Slob, Physical Review Letters, *Green's function retrieval and Marchenko imaging in a dissipative acoustic medium*, **116**, 164301-1-164301-6 (2016).